

Nanostructures

Self-assembly Mechanism and Chiral Transfer in CuO Superstructures

Jun Zhang,* Renaud A. L. Vallée,* Zdravko Kochovski, Wei Zhang, Chen Shen, Florian Bertram, and Nicola Pinna*

Abstract: Chiral inorganic superstructures have received considerable interest due to the chiral communication between inorganic compounds and chiral organic additives. However, the demanding fabrication and complex multilevel structure seriously hinder the understanding of chiral transfer and self-assembly mechanisms. Herein, we use chiral CuO superstructures as a model system to study the formation process of hierarchical chiral structures. Based on a simple and mild synthesis route, the time-resolved morphology and the in situ chirality evolution could be easily followed. The morphology evolution of the chiral superstructure involves hierarchical assembly, including primary nanoparticles, intermediate bundles, and superstructure at different growth stages. Successive redshifts and enhancements of the CD signal support chiral transfer from the surface penicillamine to the inorganic superstructure. Full-field electro-dynamical simulations reproduced the structural chirality and allowed us to predict its modulation. This work opens the door to a large family of chiral inorganic materials where chiral molecule-guided self-assembly can be specifically designed to follow a bottom-up chiral transfer pathway.

ality was discovered in a few inorganic materials due to their intrinsic crystal structures, such as quartz,^[5] mercury sulfide,^[6] and tellurium.^[7] In addition, chiral additives (e.g., chiral molecules,^[8] chiral templates,^[9] chiral light^[10]) can also induce chirality in intrinsically non-chiral inorganic compounds as well. The chirality from chiral additives is retained in the pure inorganic crystal or structure, even after the removal of the chiral additives.^[8b,11] Typically, chiral inorganic shapes can be trimmed by chiral additives following a bottom-up assembly process,^[12] which usually requires one or more fabrication steps.^[13] One-step methods for synthesizing chiral superstructures are very complex and versatile,^[13a] as they involve the complex competition among various interaction forces. Mild solution synthesis offers an opportunity to combine in situ and ex situ characterization for the assembly process. For chiral inorganic superstructure formed in solution, the chirality usually arises from differential growth rates of chiral facets or screw dislocation of crystal nuclei.^[11,14]

For molecule-guided self-assembly, chiral molecules are involved in the whole bottom-up assembly process by activating the chiral assembly, in which the molecular chirality is transferred to the non-chiral inorganic phase and eventually amplified in the chiral superstructures. Normally, only the final superstructure morphology or part of intermediates can be characterized in detail by electron microscopy or other techniques.^[15] The absence of the intermediate information will prevent a clear elucidation of the mechanism of chiral transfer and self-assembly of the superstructure. The mechanism for complex superstructure formation could be uncovered by in situ characterization or a combination of in situ and ex situ characterization. The

Introduction

Chiral inorganic superstructures have attracted considerable interest due to their wide applications in chiral resolution,^[1] optical display,^[2] biosensing,^[3] and chiral catalysis.^[4] Chir-

[*] Dr. J. Zhang
Wenzhou Institute, University of Chinese Academy of Sciences
325000 Wenzhou (China)

and
School of Physical Sciences, University of Chinese Academy of Sciences

100049 Beijing (China)
E-mail: junzhang.chem@outlook.com

Dr. R. A. L. Vallée
Univ. Bordeaux, CNRS, CRPP, UMR 5031
33600 Pessac (France)
E-mail: renaud.vallee@u-bordeaux.fr

Dr. Z. Kochovski
Department for Electrochemical Energy Storage, Helmholtz-Zentrum Berlin für Materialien und Energie
14109 Berlin (Germany)

Dr. J. Zhang, Dr. W. Zhang, Prof. N. Pinna
Institut für Chemie and IRIS Adlershof, Humboldt-Universität zu Berlin
12489 Berlin (Germany)

E-mail: nicola.pinna@hu-berlin.de

Dr. J. Zhang, Dr. C. Shen, F. Bertram
Deutsches Elektronen-Synchrotron DESY
Notkestr. 85, 22607 Hamburg (Germany)

© 2023 The Authors. Angewandte Chemie published by Wiley-VCH GmbH. This is an open access article under the terms of the Creative Commons Attribution Non-Commercial NoDerivs License, which permits use and distribution in any medium, provided the original work is properly cited, the use is non-commercial and no modifications or adaptations are made.

chiral film on a solid substrate involves controlling precise atomic arrangements to ensure highly ordered crystal growth.^[16] The formation of chirality in a solution is achieved by inducing the self-assembly of multilevel chiral units or intermediates, which opens up many possibilities for a hierarchical self-assembled superstructure.

Herein, we propose a mild aqueous-phase synthesis of CuO superstructures based on penicillamine as a chirality promoter. The CuO superstructures exhibit strong chirality, which is present even after the removal of the chirality promoters. In situ circular dichroism (CD) spectra and ex situ transmission electron microscopy (TEM) were used to follow the evolution of chirality and shapes during the formation of the chiral superstructures. Fourier transform infrared spectroscopy (FTIR) gave further insights into coordination chemistry, which, in combination with CD signals, demonstrated the chiral transfer of penicillamine between the building blocks. We have also performed a three-dimensional reconstruction of the CuO superstructures by TEM tomography that clearly shows the interpenetrating bundles with chiral rotation. Full-field electro-dynamical simulations supported our findings and allowed us to further tune and optimize the chiral response of the CuO superstructures. We also compared the assembly of CuO nanoparticles synthesized in the presence of penicillamine, cysteine, valine, mercaptobenzoic acid, and thiophenol. This was done in order to understand the role of different functional groups on superstructure formation and chiral response, as well as to reveal clear structure-property correlations.

Results and Discussion

Chiral CuO superstructures were synthesized through an aqueous solution-based method using penicillamine enantiomers and citrates as symmetry-breaking agents and structure stabilizers, respectively. The detailed procedure is described in the experimental section. Scanning electron microscopy (SEM) images showed that the as-synthesized CuO superstructures have a uniform flower-like morphology with diameters ranging from 350 to 550 nm (Figure 1a₁ & S1a, b). The flower-like superstructures consist of several crossed bundles, and the secondary bundle is assembled from a large number of ≈ 3 nm nanoplatelets (Figure 1a₂–a₃ & S1c–f). Within a nanoplatelet, primary nanoparticles can be discerned in high-resolution TEM images. The chiral CuO superstructures exhibit an antipodal chiroptical activity (Figure 1c), displaying solid CD bands at ≈ 450 nm (S_1) and ≈ 680 nm (S_2). A similar flower-like morphology was also obtained using racemic penicillamine (Figure S2a), but in this case, no chiral bands can be observed in its CD spectra (Figure S2b).

The chiral CuO superstructures have a mass fraction of organic stabilizers of $\approx 8.2\%$, as estimated from the thermogravimetric analysis (Figure S3a). The FTIR spectra of the superstructures exhibit the most prominent absorptions in the 3700 – 2800 cm^{-1} and 1800 – 1200 cm^{-1} regions, which are attributed to overlap signals of amine, hydroxyl, and carboxyl group, and disappear after calcination at 350°C due to the decomposition of the organic molecules (Figure S3b). The SEM and TEM images (Figure 1b₁, b₂ &

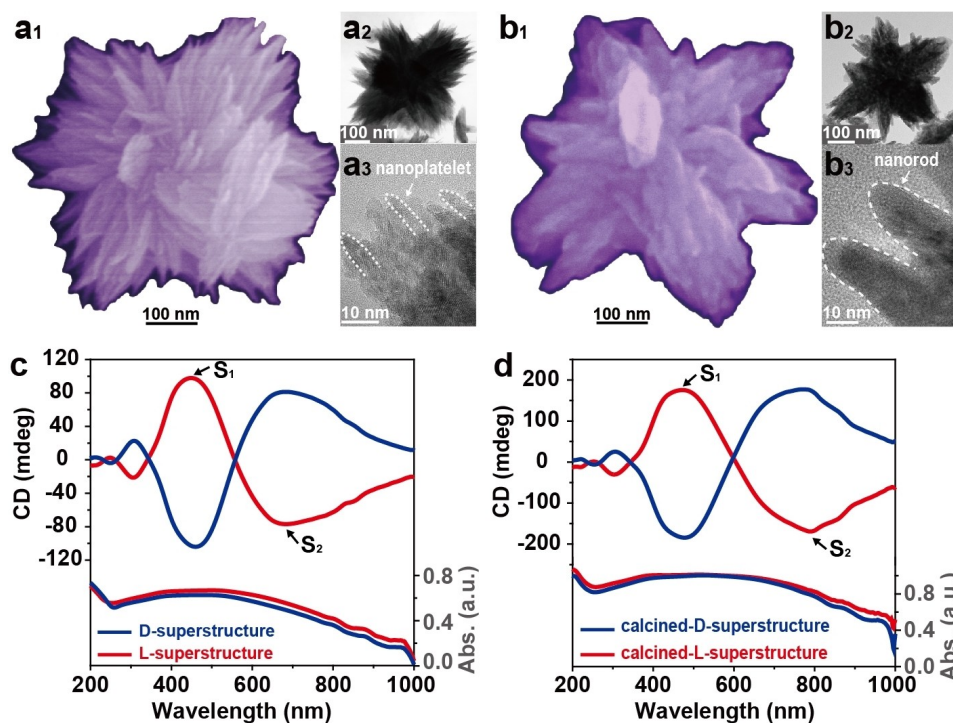


Figure 1. a) As-synthesized L-superstructures: a₁) SEM image, a₂) TEM image, and a₃) high-resolution TEM image. b) Calcined L-superstructures: b₁) SEM image, b₂) TEM image, and b₃) high-resolution TEM image. The CD and UV/Vis absorption spectra of c) the as-synthesized chiral superstructures and d) the calcined chiral superstructures.

S4a–d) of the calcined superstructures also showed flower-like shapes, indicating that the calcination step does not damage the morphology. Also, the CD signals of the calcined superstructures are maintained (Figure 1d), with the strong S_1 and S_2 CD signals slightly shifting to ≈ 480 nm and ≈ 780 nm, respectively. It should be noted that the nanoplatelets in secondary bundles have increased from 3 nm to more than 10 nm in diameter after calcination (Figure 1b₃ & S4e, f), suggesting that the superstructure chirality is fixed in the flower-like top structure. The X-ray diffraction patterns before and after calcination can be indexed to the monoclinic crystal structure of CuO (JCPDS cards, No. 48-1548, Figure S5). The selected area electron diffractions also display the characteristic reflections of CuO (Figure S1 g, h & S4g, h).

The UV/Visible spectra of the as-synthesized superstructure exhibit broad absorptions from 250 nm to 900 nm (Figure 1c). To eliminate any potential signal broadening caused by scattering, we further test the UV/Visible diffuse reflectance spectroscopy of the chiral superstructure (Figure S6). These signals can be grouped as i) signals below 320 nm belong to the charge transfer of $\text{Cu}^{2+} \leftarrow \text{O}^{2-}$; ii) the bands at 320 nm and 440 nm are attributed to the charge transfer of $\text{Cu}^{2+} - \text{O}^{2-} - \text{Cu}^{2+}$; iii) the bands above 600 nm are attributed to d-d transitions of Cu^{2+} .^[13] The antipodal CD spectra for L-superstructures and D-superstructures are clearly distinguished as the negative and positive Cotton effects. The CD signal of the as-synthesized superstructures (Figure 1c) exhibits a weak signal at ≈ 305 nm and two opposite strong signals at ≈ 450 nm and ≈ 680 nm. The Cotton effect signals centered at ≈ 341 nm and ≈ 558 nm are attributed to the charge transfer transition of $\text{Cu}^{2+} - \text{O}^{2-} - \text{Cu}^{2+}$ and d-d transitions of Cu^{2+} , respectively. The Cotton effect signal centers of the calcined superstructures are redshifted to ≈ 342 nm and ≈ 598 nm (Figure 1d) due to the increased size of the primary particles,^[16a] and their UV/Vis spectra are accompanied by a redshift. These findings support the conclusion that the chiral activity of the superstructures is unaffected by the degradation of the penicillamine and is, therefore, still observed in the pure inorganic phase.

We conducted an in-depth investigation of the assembly process to reveal the evolution of chirality and formation for the chiral superstructures. In situ CD tests allow us to visualize chiral changes due to the formation of superstructures, and are feasible in our mild solution-phase synthesis. In situ CD spectra captured during chiral superstructure assembly show a perfect symmetric evolution (Figure 2a₁, a₂). CD signals for L-superstructure and D-superstructure gradually redshift and intensify. Also, the absorption intensity of in situ UV/Visible spectra from 300 to 900 nm increases gradually over the reaction time due to superstructure formation (Figure 2b₁, b₂). The final CD spectra are completely different from the initial state, supporting that they come from the superstructure. The redshift and enhancement of the CD signal evolution allowed for a clearer understanding after deducting the initial CD signal (Figure S7). The strongest S_1 bands shifted from ≈ 370 to ≈ 555 nm and enhanced from ≈ 25 to

≈ 270 mdeg. To track the starting point of the superstructure formation, time-resolved intermediates can be separated from the reaction solution by centrifugation. The CD spectra of intermediate samples are similar to S_1 and S_2 bands, slightly redshifted after 20 mins (Figure S8a₁, a₂), but the intermediate sample obtained at 10 mins shows different CD signals (black lines), implying that the chiral superstructure starts to form between 10 and 20 mins. We selected D-superstructure as an example to illustrate its formation details using TEM. A chiral superstructure with a well-defined flower-like shape can be observed after 20 mins (Figure S8c₁–c₆). The crystallinity evolution, as shown in x-ray wide-angle scattering (WAXS) at different reaction times, is closely related to the superstructure formation (Figure S9). The in situ CD tests showed nearly identical spectra in the first 15 mins (Figure S10a). Therefore, we further examined the TEM images of intermediates to clarify the changes during this period. Figure S10b₁, b₂ show that only discrete nanoparticles with a diameter of ≈ 2.5 nm were formed in large quantities between 3 mins and 10 mins. In addition, we observed a large number of primary bundles (marked by red arrows in Figure S10c₁, c₂), which are hardly observed after 20 mins due to their further growth into superstructure or being hidden in superstructures (marked by the white dashed circle in Figure S8c₁–c₆). The different stages of primary bundles are also obviously observed (Figure S10c₁, c₂), and both superstructures and primary bundles are assembled from nanoparticles as building blocks (Figure S10c₃, c₄).

We discovered that the formation of chiral superstructures proceeds through two main processes (Figure S11): nanoparticle formation and superstructure formation. Within the first 10 mins, a large number of discrete nanoparticles are formed from reaction precursors. Once the concentration of nanoparticles exceeds the critical aggregation concentration, they aggregate into intermediate bundles following nonclassical crystallization (Figure S10c₁–c₃).^[17] The extra bundles will develop on the intermediate bundles to form the flower-like superstructure using nanoparticles as building blocks in a short time. The middle part of the primary bundle provides more contact sites and allows the building nanoparticle to give up its center of mass easily to obtain a common center of mass with the bundle.^[18a] Such formation modes ensure that the aggregation free energy is sufficient to pay the entropic price due to their thermodynamic trade-off. Here, the free-energy landscape taking place during superstructure formation determines the thermodynamic preference for the structure, shape, and size distribution of assemblies.^[18] The formation of CuO superstructures shows a well-defined and finite spatial extent in three dimensions, which is in line with the typical characteristic of self-limiting assembly with open boundaries.^[18a] It should be noted that intermediate bundles, as transition states of the superstructure, are difficult to find in the final product (Figure S8c₆). Based on this formation mechanism, we found that additional sodium hydroxide leads to an increase in the final flower-like superstructure size by growing secondary bundles (Figure S12a₁–c₁) due to increasing the number of primary nanoparticles. Here, we have

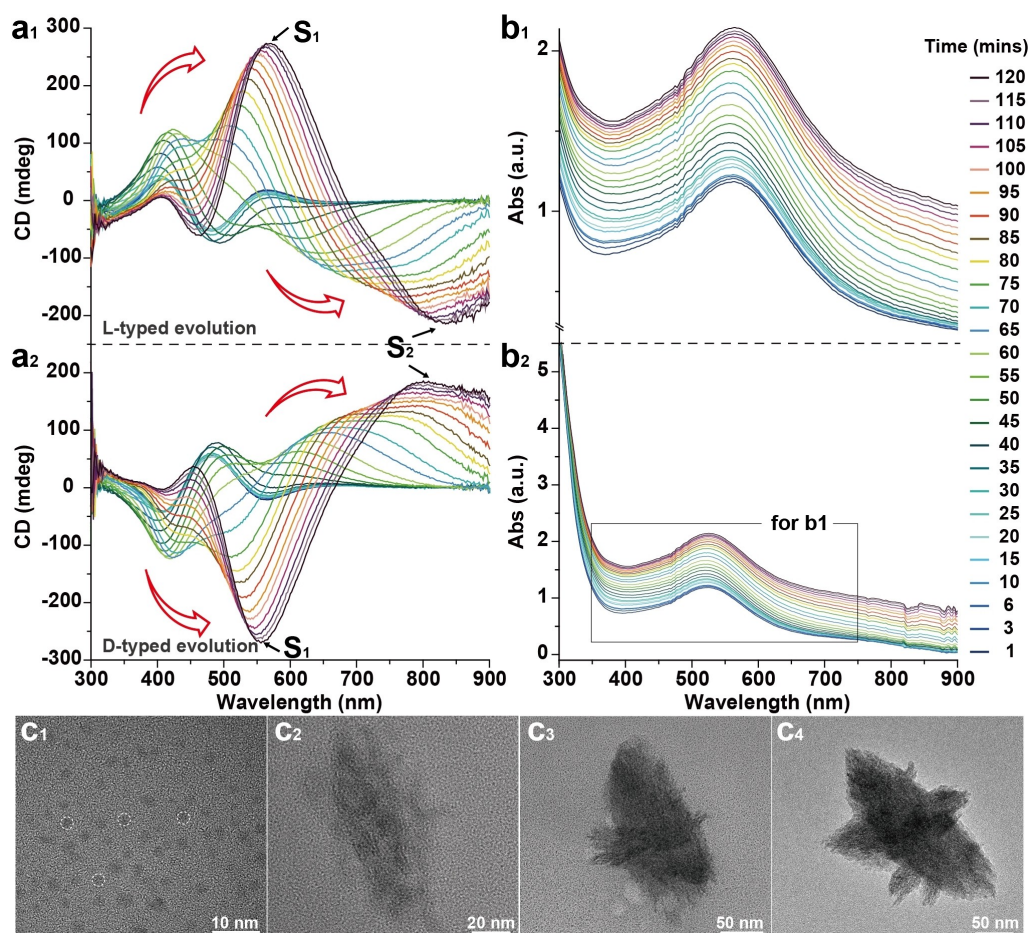


Figure 2. In situ CD spectra of a₁) L-superstructures and a₂) D-superstructures. In situ UV/Visible spectra of D-superstructures: b₁) enlarged spectra and b₂) full-range spectra. c₁)–c₄) TEM images of D-superstructure formation at different growth stages.

traced the complete formation, where primary nanoparticles act as building blocks to form the intermediate bundles and further develop superstructures (Figure 2c₁–c₄, please find more details in Figure S13). We also found that the assembly mode at 50 °C (Figure S14) is comparable at 30 °C and 70 °C (Figure S15).

Because the chirality of the CuO superstructures originates from penicillamine enantiomers, coordination chemistry plays an important role in linking chiral penicillamine and multiscale building blocks. Penicillamine can coordinate with inorganic components using sulfhydryl (–SH), carboxyl (–COOH), or amino (–NH₂) groups.^[19] We used FTIR to gain insights into the transformation of coordination patterns from primary nanoparticles to chiral superstructures. The stretching vibrations of –SH at 2607 cm^{–1} and 2512 cm^{–1} disappeared after the formation of primary nanoparticles and chiral superstructures (Figure 3a, b & Figure S16a, c, and d), suggesting that –SH groups are involved in the coordination with inorganic nanoparticles and superstructures. For primary nanoparticles, –NH₂ groups are positively charged as –NH₃⁺ at 3242 cm^{–1} (blue line in Figure 3a & S16c). Conversely, –NH₂ is immobilized on the superstructure surface as H-bonded NH, which is

evident from the broad band in the range of 3000–3650 cm^{–1} (blue line in Figure 3b & S16d).

Citrate participates in coordination bonds through the hydroxyl (–OH) and –COOH groups. Nanoparticles only coated with citrate show a broad band centered at ≈3380 cm^{–1} as H-bonded OH (red line in Figure 3b). –COOH groups are also engaged in the asymmetric stretching vibration at 1578 cm^{–1} and symmetric stretching vibration at 1387 cm^{–1} (Figure S16b). When both penicillamine and citrate are coated on the nanoparticle or the superstructure surfaces, the asymmetric (1570 cm^{–1}) and symmetric stretching vibration (1380 cm^{–1}) indicates that –COOH is involved in chemical coordination. The single broad band between 3000–3650 cm^{–1} in the superstructures shows the overlap signals of H-bonded NH and H-bonded OH.^[20] Based on these findings, we can conclude that the –SH and –COOH groups are involved in the surface coordination of nanoparticles and superstructures. Herein, penicillamine and citrate compete in terms of coordination chemistry. When the ratios of penicillamine and citrate are adjusted to 1:1, 1:2 and 1:3, the initial nanoparticle coordination provided by the two ligands leads to the formation of the assembly with different shapes and chirality (Figure S17).

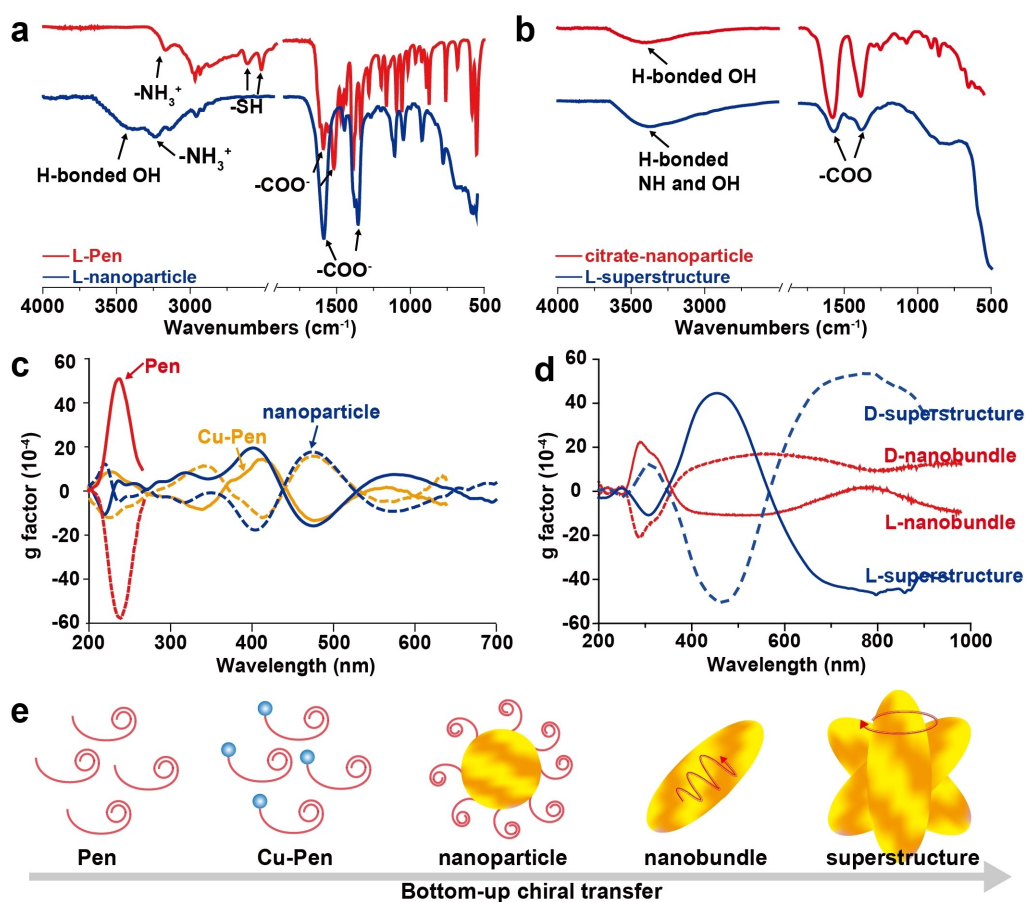


Figure 3. a) FTIR spectra of L-penicillamine (L-Pen) and L-nanoparticle. b) FTIR spectra of nanoparticles coated with only citrate (citrate-nanoparticle) and L-superstructures. c) G-factor curves of chiral penicillamine, chiral Cu-Pen complex, and chiral nanoparticles. d) G-factor curves of the ellipsoid-like bundle and chiral superstructure. e) Schematic diagram of chiral transfer for the chiral superstructure.

We further analyzed the chiroptical activity of the building blocks, including chiral penicillamine, Cu-penicillamine complexes (Cu-Pen), pure bundles, and chiral nanoparticles. Chiral penicillamine mainly contributes to the absorption peak in the ultraviolet region below 260 nm, and their CD signals show a symmetrical peak at ≈ 225 nm (Figure S18a). Chiral Cu-Pen complexes are formed from penicillamine and Cu²⁺ and are evidenced by nuclear magnetic resonance (NMR) spectra. Here, ¹H NMR, ¹³C NMR, and ¹H-¹³C HSQC showed free penicillamine (red arrow) and Cu-Pen complexes (orange arrow) in the reaction solution (Figure S19). The Cu-Pen contributed to several new CD absorption bands (e.g., ≈ 410 nm, ≈ 480 nm, and ≈ 560 nm) (Figure S18b), suggesting chiral transfer from the penicillamine molecules to the Cu-Pen. Furthermore, chiral nanoparticles exhibit an absorption peak at ≈ 520 nm in UV/Vis spectra and CD bands similar to chiral Cu-Pen from 350 to 650 nm (Figure 3c & Figure S18b), indicating that chiral penicillamine was anchored on the nanoparticle surface. Chiral nanoparticles assembled into chiral superstructures transfer surface-induced chirality to structural chirality and show that surface penicillamine activates the chiral assembly of discrete nanoparticles. Notably, intermediate bundles were observed at a reaction temperature of

50 °C (Figure S10c₁, c₃), but pure bundles are difficult to obtain due to further superstructure formation within a short time. By reducing the reaction temperature, we successfully capture the intermediate bundles (Figure S20a₁, a₂ & S20b₁, b₂). The ellipsoid-like bundles exhibit a symmetrical chirality (Figure S20c), which is different from that of the chiral superstructure even though they are coated by the same chiral molecules (Figure 3d), also underlying that the chirality of the superstructure comes from the arrangement of secondary bundles (Figure 3e).

Chiral CuO superstructures are composed of secondary bundles with a well-documented hierarchical structure (Figure S13). We marked the secondary bundles with three arrows, as three bundles can generate chirality. The largest primary bundles are designated as the rotation axis. The nearest secondary (extra) bundle to the top of the primary bundle is designated as the 1st bundle, while the second nearest secondary bundle is referred to as the 2nd bundle. If the 2nd bundle is positioned counterclockwise with regard to the 1st bundle on the rotation axis (primary bundle), it is specified as a counterclockwise rotation (L-typed, Figure S21a₁–a₃); if the 2nd bundle is located clockwise with respect to the 1st bundle, it is designated as a clockwise rotation (D-typed, Figure S21b₁–b₃). In addition, a three-

dimensional reconstruction of the CuO superstructures was carried out by TEM tomography to improve the understanding of the superstructure chirality. A supplementary video of the tilt series of TEM images clearly shows the interpenetration arrangement of the secondary bundles (Movie S1). To clearly show the details of bundle rotation at different angles, we extracted a series of TEM images of the superstructure at the rotation angle of 0° – 84° (Figure S22). These obtained TEM images rotate nearly counterclockwise around the primary bundle, and the 1st bundle is located in the counterclockwise direction with respect to the 2nd bundle. Therefore, the superstructure follows clockwise rotation also marked in tomographic reconstruction (Figure 4a₁–a₃). It should be noted that the superstructure chirality is completely different from the chirality observed in pure bundles (Figure 3d), further suggesting it arises from the chiral arrangement of secondary bundles.

Therefore, we also performed computational simulations to understand their structural chirality. Based on the three-dimensional structures, the secondary bundle is simplified to an ellipsoid that is the shape of the pure bundle. The simplified superstructure can be considered as an assembly of three ellipsoids disposed one on top of the other, further rotated by 45° with respect to each other (Figure 4b). The incident light was sent perpendicular to the main axis of the ellipsoid (along z), and a cubic mesh with a resolution of 5 nm was ensured to provide a good convergence of the CD observable. The simulated CD signals S_1 and S_2 appear at ≈ 472 nm and ≈ 680 nm (Figure 4c), and they are in good agreement with our experimental CD results (Figure 1c). They also confirm that the structural chirality of the superstructure comes from the chiral arrangement of the secondary bundles.

In addition, we further used computational simulation to predict changes in the optical activity of the superstructures.

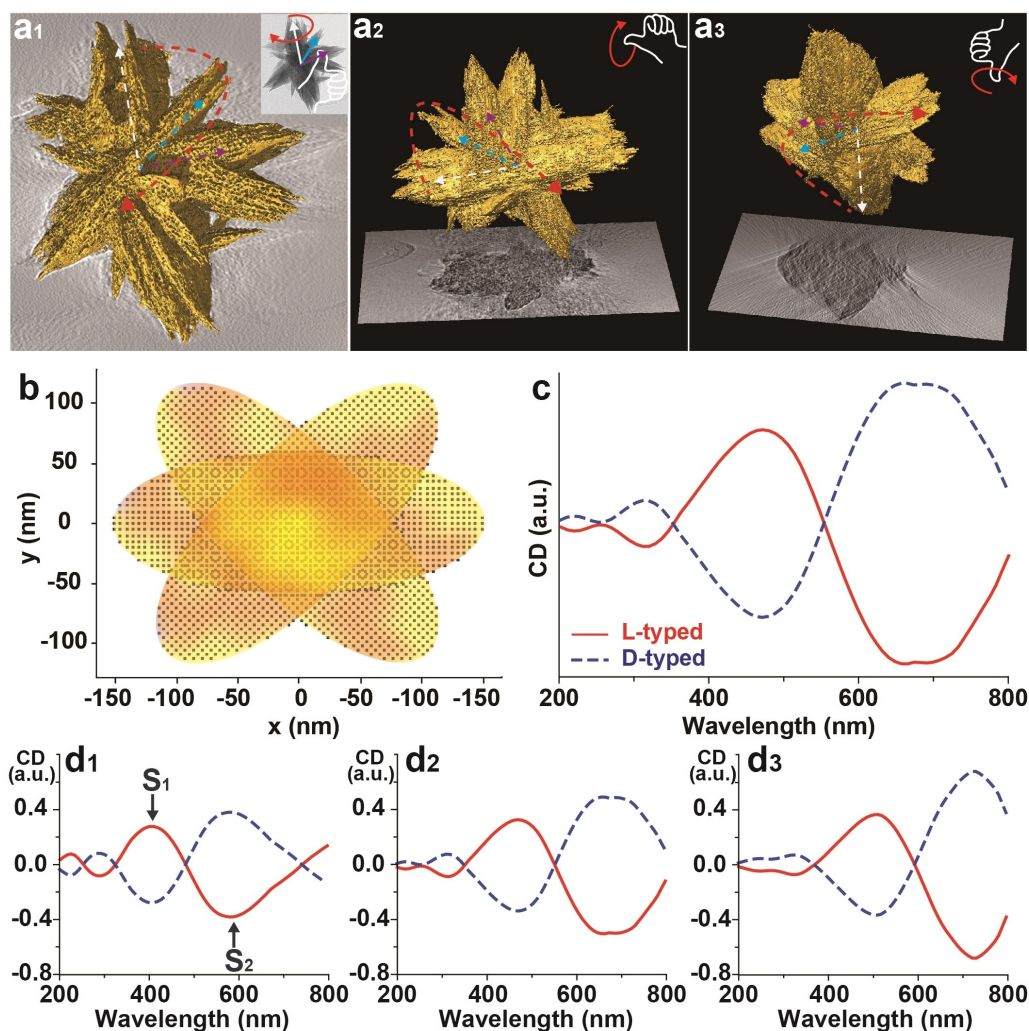


Figure 4. 3D volume renderings from an electron tomographic reconstruction of a CuO superstructure, a₁) shown over a central XY slice (corresponding TEM image in the inset) and a₂), a₃) at different orientations of the tomographic reconstruction. White arrows represent the primary bundle; blue and purple arrows are for secondary bundles. b) Simulated model and c) CD spectra of three ellipsoids with their a -axis/ b -axis/ c -axis parameter using 150/57/57 nm. Three ellipsoids are rotated 45° from each other. Simulated CD spectra of three ellipsoids with a -axis/ b -axis/ c -axis of d₁) 150/45/45 nm, d₂) 150/57/57 nm, and d₃) 150/65/65 nm.

For the ellipsoid, the *a*-axis represents its long half-axis, and the *b*-axis and *c*-axis represent its short half-axis. The adjusted ellipsoid sizes in the simplified superstructure for the *a*-/*b*-/*c*-axis were chosen to be 150/45/45 nm, 150/57/57 nm, and 150/65/65 nm, accounting for the change in the size of the secondary bundle in the CuO superstructures. As the size of the ellipsoid increases, the CD intensity of the superstructure increased from ≈ 0.38 , ≈ 0.49 to ≈ 0.68 for S_2 , and corresponding CD bands redshifted from ≈ 575 nm, ≈ 655 nm to ≈ 725 nm for S_2 . A similar trend can also be observed for S_1 , as shown in the simulated CD spectra (Figure 4d₁–d₃). Hence, it can be concluded that changing the CuO superstructure size can lead to enhanced chiroptical activity and a shift in the CD absorption peaks. Given the fact that CD measurements were performed in a solution, the CD signal exhibited by our idealized model system must be averaged over all incident angles. We performed these calculations (please see details of the averaging process in Figure S23) in the case of the L-typed system of three ellipsoids with their *a*-axis/*b*-axis/*c*-axis

parameters set to 150/45/45 nm. It turns out that the averaged CD features (blue line in Figure S23b₂) manifest simply as a small shift and broadening of the CD peaks obtained in the case of the unidirectional *z*-oriented beam shown in Figure 4d₁, thus fully supporting our analysis.

Thanks to the computational simulations, we know how the modulation of the superstructure size controls the chiroptical activity. By adjusting the reaction temperature to 30 °C, 50 °C, and 70 °C, the superstructures gradually increase in size due to the growth of the secondary bundle size (Figure 5a₁–c₁). We used the anisotropy factor (*g*-factor) to evaluate chiral activity to avoid concentration dependence. *G*-factor of charge transfer for $\text{Cu}^{2+}\text{-O}^{2-}\text{-Cu}^{2+}$ (S_1) increased from ≈ 0.003 to ≈ 0.007 , and d-d transitions of Cu^{2+} (S_2) also grew from ≈ 0.004 to ≈ 0.006 (Figure 5a₂–c₂). The S_1 moved from ≈ 392 nm to ≈ 497 nm, and S_2 shifted from ≈ 565 nm to ≈ 785 nm. The redshifted and enhanced CD signal supports the prediction from the computational simulations.

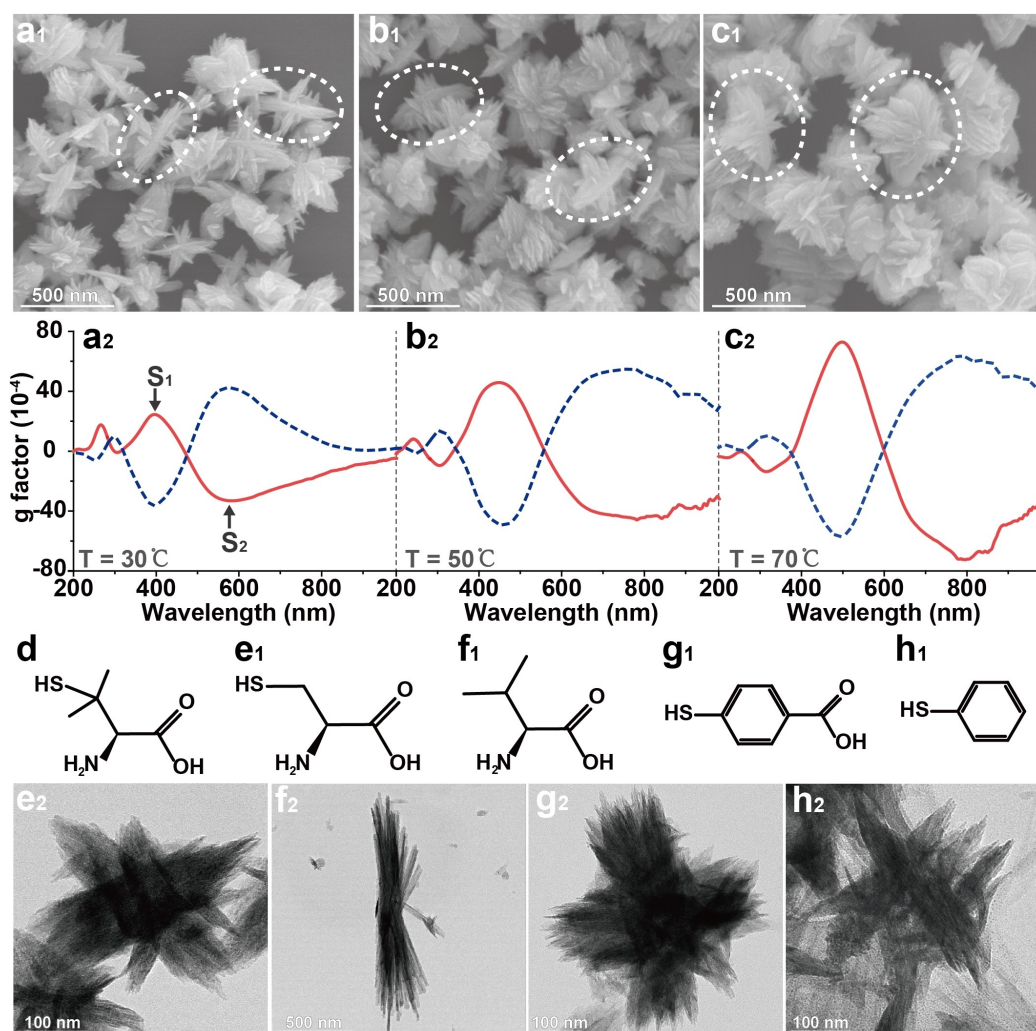


Figure 5. a₁)–c₁) SEM images and a₂)–c₂) *g*-factor curves of chiral superstructures synthesized at a) 30 °C, b) 50 °C, and c) 70 °C. d) Molecular structure of penicillamine; e₁)–h₁) molecular structures of e) cysteine, f) valine, g) mercaptobenzoic acid, and h) thiophenol, and e₂)–h₂) the TEM images of their corresponding assemblies.

To better understand the chiral transfer, we investigated the superstructure formation starting from pure bundles. The hydrothermal reactions at 120 °C led to the formation of flower-like superstructures (Figure S24) from pure bundles (Figure S20a₁–b₁). Interestingly, the resulting superstructures starting from the pure bundles were found to be achiral, in contrast to the chiral superstructures obtained from chiral nanoparticles (Figure S25). We assume that the higher temperature required for the bundles to assemble into the superstructures may break the coordination interaction of chiral penicillamine leading to a failure of the chiral transfer. Therefore, although higher temperature permits the formation of superstructures, the chiral transfer from surface penicillamine is being lost. Indeed, we conducted experiments without penicillamine, which resulted in the formation of achiral bundle-like assemblies instead of superstructures (Figure S26).

However, with the addition of penicillamine, chiral superstructures were formed at the same temperature (Figure S1a–d), demonstrating that the penicillamine ligands did reduce the temperature required for superstructure formation while maintaining their chiral properties. In addition, we used four additional molecules replacing chiral penicillamine to study their effect on the assembly. Cysteine, which has a similar molecular structure and functional groups as penicillamine (Figure 5d & e₁), was found to successfully produce CuO superstructures (Figure 5e₂ & S27a). Also, enhanced chiroptical activity and tunable CD absorption bands were observed for the chiral superstructures using cysteine enantiomers at reaction temperatures from 30 °C, 50 °C, to 70 °C (Figure S28). Valine, which also has a similar molecular structure to penicillamine (Figure 5f₁), resulted in the formation of pure bundles (Figure 5f₂ & S27b) due to the absence of the –SH group. Although the pure bundles are similar to the structures obtained without penicillamine, we found that the bundles using valine enantiomers are chiral (Figure S29). Mercaptobenzoic acid and thiophenol are, on the other hand, able to produce similar superstructures (Figure 5g, h, S27c, and d). Thus, one can safely conclude that chiral molecules bearing –SH groups are needed for the superstructure formation.

Conclusion

We have successfully introduced a bottom-up chiral transfer from chiral molecules to high-order flower-like CuO superstructures. After the removal of the chiral molecules, the chirality is still present in the pure inorganic superstructures. We found that the evolution of the morphology and chirality for the superstructures is closely related to the growth of extra bundles from the initial bundle resulting in a chiral flower-like structure. The superstructure formation is strongly dependent on the coordination chemistry of the chiral ligands used. The chiral interpenetration of the bundles for superstructures is clearly shown by the 3D reconstruction. The full-field electro-dynamical simulations were further used to model their chiroptical activity and successfully predict chirality changes. The tunable structural

chirality from visible to near-infrared bands can be controlled by the coordination chemistry, precursor dosage, and reaction temperature through modulation of the size and morphology of the superstructure. This work provides a new simple approach for designing and assembling a new generation of chiral inorganic nanomaterials following a simple bottom-up method using chiral molecules.

Acknowledgements

We acknowledge technical support from the SPC facility at EMBL Hamburg. We acknowledge DESY (Hamburg, Germany), a member of the Helmholtz Association HGF, for the provision of experimental facilities. Parts of this research were carried out at PETRA III. We would like to thank Dr Felix Lehmkuhler and Anca Simona Ciobanu for assistance in using the chemistry lab, and Dr Björn Kobin and Dr Angelica Struve Garcia for using the CD spectrometer. We greatly thank Christoph Erdmann for part of the TEM measurements. J. Zhang acknowledges support from National Natural Science Foundation of China (Grant No. 22005303) and Helmholtz-OCPC Postdoc Program (No. ZD2022010). Open Access funding enabled and organized by Projekt DEAL.

Conflict of Interest

The authors declare no conflict of interest.

Data Availability Statement

The data that support the findings of this study are available from the corresponding author upon reasonable request.

Keywords: Chiral Transfer · CuO Superstructure · Self-Assembly · Structural Chirality

- [1] a) B. Ni, H. Cölfen, *SmartMat* **2021**, *2*, 17–32; b) Z. Sun, J. Hou, L. Li, Z. Tang, *Coord. Chem. Rev.* **2020**, *425*, 213481.
- [2] D.-W. Zhang, M. Li, C.-F. Chen, *Chem. Soc. Rev.* **2020**, *49*, 1331–1343.
- [3] C. Hao, L. Xu, H. Kuang, C. Xu, *Adv. Mater.* **2020**, *32*, 1802075.
- [4] M. Sun, L. Xu, A. Qu, P. Zhao, T. Hao, W. Ma, C. Hao, X. Wen, F. M. Colombari, A. F. de Moura, N. A. Kotov, C. Xu, *Nat. Chem.* **2018**, *10*, 821–830.
- [5] R. M. Hazen, D. S. Sholl, *Nat. Mater.* **2003**, *2*, 367–374.
- [6] a) P. P. Wang, S. J. Yu, A. O. Govorov, M. Ouyang, *Nat. Commun.* **2017**, *8*, 14312; b) K. Ishito, H. Mao, Y. Kousaka, Y. Togawa, S. Iwasaki, T. Zhang, S. Murakami, J.-i. Kishine, T. Satoh, *Nat. Phys.* **2023**, *19*, 35–39.
- [7] a) A. Ben-Moshe, A. D. Silva, A. Müller, A. Abu-Odeh, P. Harrison, J. Waelder, F. Niroui, C. Ophus, A. M. Minor, M. Asta, W. Theis, P. Ercius, A. P. Alivisatos, *Science* **2021**, *372*, 729–733; b) F. Calavalle, M. Suárez-Rodríguez, B. Martín-García, A. Johansson, D. C. Vaz, H. Yang, I. V. Maznichenko,

- S. Ostanin, A. Mateo-Alonso, A. Chuvilin, *Nat. Mater.* **2022**, *21*, 526–532.
- [8] a) W. Jiang, Z.-B. Qu, P. Kumar, D. Vecchio, Y. Wang, Y. Ma, J. H. Bahng, K. Bernardino, W. R. Gomes, F. M. Colombari, *Science* **2020**, *368*, 642–648; b) B. Ni, M. Mychinko, S. Gómez-Graña, J. Morales-Vidal, M. Obelleiro-Liz, W. Heyvaert, D. Vila-Liarte, X. Zhuo, W. Albrecht, G. Zheng, *Adv. Mater.* **2023**, *35*, 2208299; c) B. Ni, J. Zhou, L. Stolz, H. Cölfen, *Adv. Mater.* **2023**, *35*, 2209810; d) G. Otis, M. Nassir, M. Zutta, A. Saady, S. Ruthstein, Y. Mastai, *Angew. Chem. Int. Ed.* **2020**, *59*, 20924–20929.
- [9] a) D. Vila-Liarte, N. A. Kotov, L. M. Liz-Marzan, *Chem. Sci.* **2022**, *13*, 595–610; b) D. Wu, K. Zhou, J. Tian, C. Liu, J. Tian, F. Jiang, D. Yuan, J. Zhang, Q. Chen, M. Hong, *Angew. Chem. Int. Ed.* **2021**, *60*, 3087–3094.
- [10] C. Hao, G. Wang, C. Chen, J. Xu, C. Xu, H. Kuang, L. Xu, *Nano-Micro Lett.* **2023**, *15*, 39.
- [11] a) G. González-Rubio, J. Mosquera, V. Kumar, A. Pedrazo-Tardajos, P. Llombart, D. M. Solís, I. Lobato, E. G. Noya, A. Guerrero-Martínez, J. M. Taboada, *Science* **2020**, *368*, 1472–1477; b) H. E. Lee, H. Y. Ahn, J. Mun, Y. Y. Lee, M. Kim, N. H. Cho, K. Chang, W. S. Kim, J. Rho, K. T. Nam, *Nature* **2018**, *556*, 360–365.
- [12] a) J. Lv, X. Gao, B. Han, Y. Zhu, K. Hou, Z. Tang, *Nat. Chem. Rev.* **2022**, *6*, 125–145; b) X. Yang, J. Lv, J. Zhang, T. Shen, T. Xing, F. Qi, S. Ma, X. Gao, W. Zhang, Z. Tang, *Angew. Chem. Int. Ed.* **2022**, *61*, e202201674.
- [13] a) Y. Duan, X. Liu, L. Han, S. Asahina, D. Xu, Y. Cao, Y. Yao, S. Che, *J. Am. Chem. Soc.* **2014**, *136*, 7193–7196; b) H. Yu, L. Wang, S. Liu, B. Zhao, K. Xiao, B. Yang, H. Duan, H. Zhao, J. Deng, *Carbohydr. Polym.* **2022**, *296*, 119944; c) Á. Coogan, L. Hughes, F. Purcell-Milton, S. Cardiff, V. Nicolosi, Y. K. Gun'ko, *J. Phys. Chem. C* **2022**, *126*, 18980–18987.
- [14] a) A. G. Shtukenberg, Y. O. Punin, A. Gujral, B. Kahr, *Angew. Chem. Int. Ed.* **2014**, *53*, 672–699; b) Y. Liu, J. Wang, S. Kim, H. Sun, F. Yang, Z. Fang, N. Tamura, R. Zhang, X. Song, J. Wen, *Nature* **2019**, *570*, 358–362.
- [15] a) T. Bai, J. Ai, Y. Duan, L. Han, S. Che, *Small* **2022**, *18*, 2104509; b) T. Bai, J. Ai, J. Ma, Y. Duan, L. Han, J. Jiang, S. Che, *Angew. Chem. Int. Ed.* **2021**, *60*, 20036–20041.
- [16] a) E. W. Bohannan, H. M. Kothari, I. M. Nicic, J. A. Switzer, *J. Am. Chem. Soc.* **2004**, *126*, 488–489; b) B. Luo, A. Banik, E. W. Bohannan, J. A. Switzer, *J. Phys. Chem. C* **2020**, *124*, 21426–21434.
- [17] M. Jehannin, A. Rao, H. Cölfen, *J. Am. Chem. Soc.* **2019**, *141*, 10120–10136.
- [18] a) M. F. Hagan, G. M. Grason, *Rev. Mod. Phys.* **2021**, *93*, 025008; b) J. J. De Yoreo, P. U. Gilbert, N. A. Sommerdijk, R. L. Penn, S. Whitelam, D. Joester, H. Zhang, J. D. Rimer, A. Navrotsky, J. F. Banfield, *Science* **2015**, *349*, aaa6760.
- [19] a) T. Long, Y. Guo, M. Lin, M. Yuan, Z. Liu, C. Huang, *Nanoscale* **2016**, *8*, 9764–9770; b) Y. Sameshima, N. Yoshinari, K. Tsuge, A. Igashira-Kamiyama, T. Konno, *Angew. Chem. Int. Ed.* **2009**, *48*, 8469–8472.
- [20] E. Pretsch, P. Bühlmann, M. Badertscher, *Structure determination of organic compounds*, Springer, Heidelberg, **2000**, pp. 287–300.

Manuscript received: April 16, 2023

Accepted manuscript online: April 26, 2023

Version of record online: May 19, 2023